Force and stepwise movements of gliding motility in human pathogenic bacterium *Mycoplasma pneumoniae*

Masaki Mizutani[a], Yuya Sasajima[a], Makoto Miyata[a,b#]

[a]Graduate School of Science, Osaka City University, 3-3-138 Sugimoto, Sumiyoshi-ku, Osaka 558-8585, Japan.

[b]The OCU Advanced Research Institute for Natural Science and Technology (OCARINA), Osaka City University, 3-3-138 Sugimoto, Sumiyoshi-ku, Osaka 558-8585, Japan.

Address correspondence to Makoto Miyata, miyata@osaka-cu.ac.jp

Present address: Masaki Mizutani: Bioproduction Research Institute, National Institute of Advanced Industrial Science and Technology (AIST), 1-1-1 Higashi, Tsukuba, Ibaraki 305-8566, Japan

Running title: Force and step of *Mycoplasma pneumoniae* gliding

Keywords: Motility, Optical tweezers, class *Mollicutes*, Infection

ABSTRACT

Mycoplasma pneumoniae, a human pathogenic bacterium, binds to sialylated oligosaccharides and glides on host cell surfaces via a unique mechanism. Gliding motility is essential for initiating the infectious process. In the present study, we measured the stall force of an *M. pneumoniae* cell carrying a bead that was manipulated using optical tweezers on two strains. The stall forces of M129 and FH strains were averaged to be 23.7 and 19.7 pN, respectively, much weaker than those of other bacterial surface motilities. The binding activity and gliding speed of the M129 strain on sialylated oligosaccharides were eight and two times higher than those of the FH strain, respectively, showing that binding activity is not linked to gliding force. Gliding speed decreased when cell binding was reduced by addition of free sialylated oligosaccharides, indicating the existence of a drag force during gliding. We detected stepwise movements, likely caused by a single leg under 0.2–0.3 mM free sialylated oligosaccharides. A step size of 14–19 nm showed that 25–35 propulsion steps per second are required to achieve the usual gliding speed. The step size was reduced to less than half with the load applied using optical tweezers, showing that a 2.5 pN force from a cell is exerted on a leg. The work performed in this step was 16%–30% of the free energy of the hydrolysis of ATP molecules, suggesting that this step is linked to the elementary process of *M. pneumoniae* gliding.

IMPORTANCE

Human mycoplasma pneumonia is caused by the bacterium *Mycoplasma pneumoniae*. This tiny bacterium, shaped like a missile, binds to human epithelial surfaces and spreads using a unique gliding mechanism to establish

infection. Here, we analyzed the movements and force of this motility using a special setup: optical tweezers. We then obtained detailed mechanical data to understand this mechanism. Furthermore, we succeeded in detecting small steps of nanometers in its gliding, which is likely linked to the elementary process of the core reaction: chemical to mechanical energy conversion. These data provide critical information to both control this human pathogen and explore new ideas for artificial molecular machines.

53 **INTRODUCTION**

54 Members of the bacterial class *Mollicutes*, which includes the genus
55 *Mycoplasma*, are parasitic and occasionally commensal bacteria that are
56 characterized by small cells and genomes and by the absence of a
57 peptidoglycan layer (1, 2). *Mycoplasma* species bind to host cell surfaces and
58 exhibit gliding motility to spread the infectious area. Interestingly, *Mycoplasma*
59 gliding does not involve flagella or pili and is completely unrelated to other
60 bacterial motility systems or conventional motor proteins that are common in
61 eukaryotic motility (3). The gliding motility of *Mycoplasma* is divided into two
62 types, *Mycoplasma pneumoniae* and *Mycoplasma mobile*, which share no
63 homology in component proteins, indicating independent mechanisms (4, 5).
64 *M. pneumoniae* is a human pathogen that causes respiratory diseases,
65 including bronchitis and atypical pneumonia (6). *M. pneumoniae* cells bind to
66 human epithelial surfaces through sialylated oligosaccharides (SOs), which are
67 major structures of animal cell surfaces related to cell-cell recognition, and the
68 binding targets of many pathogens and toxins (7-10). The cells show
69 unidirectional gliding motility at a speed of up to 1 μm/s on SO-coated glass
70 surfaces (Fig. 1A) (5, 11), which is known to be essential for their infection (12).
71 The gliding machinery, called the “attachment organelle,” is localized at a cell
72 pole (13). The attachment organelle is divided into two parts: internal and
73 surface structures. The internal structure is composed of an internal core
74 complex and a surrounding translucent area. The internal core comprises three
75 parts: a terminal button, paired plates, and a bowl complex from the front side of
76 the cell (Fig. 1B) (5, 14, 15). The major surface structure, called “P1 adhesin

complex" or "genitalium and pneumoniae cytoadhesin (GPCA)", is composed of P1 adhesin and P40/P90 proteins and aligned around the internal structure, which plays a dual role as the adhesin to bind to SOs and as the leg for gliding (Fig. 1B) (16-20). The model for gliding called the "Inchworm model" or "Double-spring hybrid ratchet model" is proposed, in which cells repeat the extensions and contractions of the attachment organelle based on the energy from ATP hydrolysis to enable smooth gliding (15, 21-23). Generally, the mechanical characteristics and detailed analysis of movements are essential for creating and completing a detailed model for the motility mechanism (24-28). However, to date, no information is available about the force for gliding.

In the present study, we measured the stall forces of the two strains and discuss the relationship between binding and force. Furthermore, we succeeded in detecting and measuring stepwise movements that are likely linked to the elementary process of the gliding reaction.

Results

Stall force measurement using optical tweezers. Optical tweezers are commonly used to measure the stall force generated by pili in bacterial motility or motor proteins in eukaryotic motility (29-32). The stall force is defined as the force needed to stop movements and is equal to the maximal propulsion force for locomotion. Previously, we measured the stall force for the gliding motility of *M. mobile*, based on a mechanism unrelated to *M. pneumoniae* gliding, using optical tweezers (33, 34). In the present study, we applied this method to *M. pneumoniae* gliding. *M. pneumoniae* cells were biotinylated and inserted into a

101 tunnel chamber, which was assembled using two glass plates and double-sided
102 tape (35). An avidin-conjugated polystyrene bead was trapped by a highly
103 focused laser beam and attached to a gliding cell at the back end of the cell
104 body by exploiting the avidin-biotin interaction. The cells pulled the bead from
105 the trap center with gliding and then stalled (Fig. 2A and B; *SI Appendix*, Movie
106 S1). The force was calculated by measuring the distance between the centers
107 of the bead and the laser trap, which was multiplied by the trap stiffness; the
108 force acting on the bead increased linearly with the displacement from the trap
109 center (29). Starting from 0 s, the pulling force increased and reached a plateau
110 in 120 s (Fig. 2C). The maximal value of the force averaged over one second
111 was determined as the stall force. The stall force of M129 strain cells was 23.7
112 ± 6.3 pN (Fig. 2E). We also measured the stall force of the FH strain, another
113 major strain of *M. pneumoniae*. The cells of the FH strain pulled the bead in a
114 manner similar to that of M129 cells (*SI Appendix*, Movie S2). The stall force of
115 the FH strain was 19.7 ± 5.3 pN, significantly weaker than that of the M129
116 strain (Fig. 2D and E).

117 **Binding activity and gliding motility.** To characterize the differences
118 in gliding motility, we measured the binding activity and gliding speed of the
119 M129 and FH strains. *M. pneumoniae* cells were suspended in HEPES
120 buffer containing 20 mM glucose to obtain an optical density at 595 nm of
121 0.07, then inserted into tunnel chambers. After incubation for 5–30 min, the
122 tunnel chambers were washed and observed by phase-contrast microscopy.
123 The number of bound cells in the M129 strain increased with time from 90 ±
124 16 to 308 ± 20 cells in 100 ×100 μm^2 area from 5 to 30 min (Fig. 3A and B).

125 These values are consistent with the results of a previous report (9). In contrast,
126 the number of bound cells in the FH strain increased from 12 ± 2 to 36 ± 8 cells
127 from 5 to 30 min (Fig. 3A and B). The number of bound cells in the FH strain
128 was 7.2–8.7-fold smaller than that of the M129 strain at all time points (Fig. 3B).
129 When 10× concentrated cell suspension was examined, the bound cell numbers
130 of the FH strain increased from 117 ± 10 to 386 ± 24 cells from 5 to 30 min, 1.2–
131 1.3 times that of M129 at all time points (Fig. 3A and B). These results indicate
132 that the FH strain has approximately 8-fold lower binding activity to SO-coated
133 glass surfaces than the M129 strain. Considering that the stall force of FH was
134 only 1.2-fold smaller than that of the M129 strain, the force is unlikely to be
135 linked to binding activity.

136 Most of the bound cells showed gliding motility on the SO-coated glass (Fig.
137 3C; *SI Appendix*, Movies S3 and S4). To characterize gliding motility, the
138 proportion of gliding cells and gliding speed were analyzed. The proportion of
139 gliding cells to all bound cells was 78.1% (n_{total} = 2284, n_{glide} = 1785) and 60.0%
140 (n_{total} = 2271, n_{glide} = 1362) in the M129 and FH strains, respectively (Fig. 3C).
141 The gliding speeds averaged for 20 s at 1-s intervals were 0.47 ± 0.08 and 0.21
142 ± 0.07 μm/s for M129 and FH strains, respectively (Fig. 3D). These results
143 suggest that binding activity is not directly linked to gliding speed.

144 **Differences in amino acid sequences of gliding proteins between two**
145 **strains.** The FH strain used in this study has not been genomically analyzed.
146 Therefore, we sequenced the genomes of both strains using MiSeq (*SI*
147 *Appendix*, Dataset S1) and analyzed the sequences of 14 genes that have been
148 reported to be involved in binding and gliding (5). Only one amino acid was

149 substituted in the M129 strain genome from a standard genome, M129-B7
150 (GenBank accession no. CP003913), which was V196A in the HMW3 protein,
151 which is positioned at the terminal button in the attachment organelle (Fig. 1B).
152 Our FH strain had 161 and 155 variations from the reported FH and FH2009
153 strains, respectively (GenBank accession no. CP010546 and CP017327),
154 indicating that the FH strain is distant from the genome strains. The differences
155 between the two strains analyzed in the present study in terms of the 14 genes
156 were as follows: (i) P1 adhesin showed many differences, including 87 single
157 amino acid substitutions, 18 amino acid insertions, and four amino acid
158 deletions, known differences of FH from M129 strains (*SI Appendix*, Fig. S1). (ii)
159 The P40/P90 protein showed 96 single amino acid substitutions, one amino
160 acid insertion, and 68 amino acid deletions (*SI Appendix*, Fig. S2). (iii) The other
161 12 genes showed 0–5 mutations in each gene, as summarized in *SI Appendix*,
162 Table S1.

163 **Effect of free sialyllactose on binding and gliding.** *M. pneumoniae* cells
164 have hundreds of legs and glide smoothly on solid surfaces. To trace the
165 behavior of a single propulsion event, the number of working legs should be
166 reduced by adding a free form of SO, which is the binding target for gliding (9,
167 34, 36). To quantitatively analyze the effects of free SO on the binding activity
168 and gliding under our conditions, we measured the bound ratio of cells and the
169 gliding speed of the M129 strain under various concentrations of the SO, 3'-*N*-
170 acetylneuraminyllactose (SL). *M. pneumoniae* cells suspended in the buffer
171 were inserted into a tunnel chamber. Then, the cell behavior in 0–0.5 mM SL
172 solutions was analyzed. The addition of free SL slowed down and then stopped

173 gliding or released the gliding cells from the glass surfaces, but did not release
174 non-gliding cells, indicating that release requires glass binding by GPCA with
175 displacements (Fig. 4A). The number of gliding cells and the gliding speed
176 relative to the initial speed were decreased by 0.1–0.5 mM with SL treatments
177 from 55 ± 11% to 26 ± 16% and from 0.33 ± 0.06 to 0.19 ± 0.07 μm/s,
178 respectively (Fig. 4B and C). We then decided to use 0.2–0.3 mM
179 concentrations for further experiments because the binding and gliding were
180 partially inhibited under these conditions, which were advantageous for
181 observing single propulsion events caused by a single leg during gliding.
182 **Stepwise gliding movements observed under free SL.** Next, we traced
183 cells under 0.2–0.3 mM free SL conditions as performed in the stall force
184 measurements. The gliding cells slowly pulled the beads from the trap center.
185 Half of the tested cells stalled in 120 s, but the other cells repeated creeping
186 movements and detachment from the glass surfaces (Fig. 5A). The stall force of
187 the cells that reached a plateau in 120 s was 16.2 ± 4.5 pN (Fig. 5B), which was
188 significantly weaker than that without SL ($p = 1.1\times10^{-5}$ by Student's *t*-test). In
189 creeping movements, cells occasionally showed discontinuous displacements,
190 which were mostly stepwise (Fig. 5C and D). Individual displacements in a
191 stepwise time course were analyzed using the pairwise distance function (34,
192 36). The displacements shown in Fig. 5D were uniformly distributed at about
193 17-, 14-, and 16-nm intervals under 0.15, 0.20, and 0.17 pN/nm of trap stiffness,
194 corresponding to 2.55, 2.80, and 2.66 pN of propulsion force, respectively (Fig.
195 5D and E). Note that force increments are generally calculated from the trap
196 stiffness × displacement (29, 34).

197 Next, to examine the load dependency of step sizes in detail, we measured step
198 sizes under 0.07–0.26 pN/nm of trap stiffness. Ninety-seven steps in 36 cell
199 trajectories, including at least two continuous steps, were detected. The step
200 sizes under 0.13 to 0.26 pN/nm of trap stiffness linearly decreased from 21.0 to
201 8.0 nm with trap stiffness (Fig. 5F and H). In contrast, the step sizes from 0.07
202 to 0.12 pN/nm of trap stiffness were mostly constant and distributed at 14–19
203 nm with an average of 16.2 ± 2.7 nm (n = 21) (Fig. 5G–I).
204 From 0.07 to 0.12 pN/nm of trap stiffness, the force increments increased with
205 the trap stiffness (Fig. 5I). In the cases where the force values increase with
206 trap stiffness, the calculated force does not reflect the actual force because the
207 load is too small to influence the movements. Therefore, we focused on the
208 force increments measured under 0.13–0.26 pN/nm of trap stiffness. The force
209 exerted in a single propulsion step was concluded to be 2.5 ± 0.3 pN (n = 76)
210 (Fig. 5J).
211

212 **Discussion**

213 ***M. pneumoniae* has weak stall force.** In the present study, we measured
214 the stall force in *M. pneumoniae* gliding using optical tweezers. Previously, the
215 stall force was measured for some bacterial surface motilities. *Neisseria*
216 *gonorrhoeae* and *Myxococcus xanthus* show surface motility driven by the
217 retraction of type IV pili (37). The stall forces of single-pilus retraction in *N.*
218 *gonorrhoeae* and *M. xanthus* were measured by optical tweezers to be
219 approximately 80 and 150 pN, respectively (30, 38). *M. mobile* glides up to 4.0
220 μm/s by a mechanism unrelated to that of *M. pneumoniae*. Previously, we

221 measured the stall force of *M. mobile* gliding using optical tweezers to be
222 approximately 113 pN (23). The stall forces of *M. pneumoniae* gliding were 23.7
223 ± 6.3 and 19.7 ± 5.3 pN in M129 and FH strains, respectively (Fig. 2E), much
224 weaker than those of other bacterial surface motilities. *M. pneumoniae* has a
225 streamlined cell body about 0.2 μm in diameter (39). This shape and cell size
226 may be beneficial for gliding in human tissues with weak forces.
227 In liquid culture, *M. pneumoniae* cells bind to the bottom surface of the
228 tissue culture flask. This is distinct from the case of *M. mobile*, in which most
229 cells float in the medium. Therefore, *M. pneumoniae* is expected to have a
230 stronger force for gliding than *M. mobile*. However, we found that *M.*
231 *pneumoniae* had a much weaker stall force than *M. mobile* (Fig. 2E). When
232 comparing the two strains of *M. pneumoniae*, the FH strain showed much less
233 active binding than, but a stall force comparable to, that of M129 (Fig. 2E and
234 3B). These facts indicate that the binding activity of *M. pneumoniae* cells is not
235 determined by the gliding force, which is represented by the stall force.
236 **Drag force in gliding.** The gliding speed decreased when cell binding was
237 partially inhibited by the addition of free SL (Fig. 4). This observation is
238 consistent with previous data; that is, the inhibition of binding by monoclonal
239 antibodies decreased the gliding speed of *M. pneumoniae* (40) and the
240 inhibition by SL decreased the speed of *M. gallisepticum*, coinciding with the
241 common mechanism with *M. pneumoniae* (23). The decrease in speed was
242 probably caused by the drag force generated from the substrate surface,
243 because the friction force exerted from water is estimated to be more than 5000
244 times smaller than the stall force of 24 pN (Fig. 2E) (41, 42). As the cause of the

245 drag force, two possibilities are considered: GPCA and others. If some
246 proportion of GPCA molecules are not involved in gliding, they are not released
247 from SOs by inhibitory factors, resulting in speed reduction. Interestingly, these
248 observations and explanations are similar to the case of *M. mobile* gliding, even
249 though they do not share the same structure of machinery (4, 9, 42-44). This
250 scheme may be advantageous for gliding on SOs based on ATP energy.

251 **Stepwise movement as elementary process.** We succeeded in detecting
252 the stepwise movements of *M. pneumoniae* gliding. *M. pneumoniae* cells glided
253 at a speed of 0.47 μm/s (Fig. 3D), and the step size in the load-free condition
254 was 14–19 nm (Fig. 5I), suggesting 25–35 steps per second. Stepwise
255 movements are well-studied in ATP-driven eukaryotic motor proteins including
256 myosin, dynein, and kinesin (26, 45). The force and displacement of a single
257 step in myosin II, cytoplasmic dynein, kinesin-1, and myosin V have been
258 reported as 3–5, 7–8, 8, and 2–3 pN and 5.3, 8, 8, and 36 nm, respectively (24,
259 29, 31, 32, 46, 47). Stepwise movements are also present in bacterial motility. A
260 flagellar motor shows 14 degrees of revolution as a step (27, 48). The gliding of
261 *M. mobile* shows stepwise movements of 1.5 pN force and 70 nm length (34,
262 36). Generally, stepwise movements are thought to correspond to the
263 elementary process of a motility event.

264 Previously, we showed that *M. pneumoniae*-type gliding motility is driven by
265 energy from ATP hydrolysis (23). Motilities driven by ATP energy can be divided
266 into elementary processes that are directly coupled with ATP hydrolysis, such as
267 stepwise movements. The elementary processes observed as steps require a
268 smaller amount of work than the energy produced by ATP hydrolysis, which is

269 ~80 pN nm (49). Therefore, we estimated the work done in the stepwise
270 movements of *M. pneumoniae* gliding to determine this possibility. The work
271 was estimated to be 18.2 ± 5.4 pN nm from the equation W_{step} = 0.5 × spring
272 constant × displacement^2, under 0.13–0.26 pN/nm of trap stiffness, where the
273 stiffness is large enough to determine the force (*SI Appendix*, Fig. S3) (34). This
274 value is 16%–30% of the free energy of the hydrolysis of ATP molecules,
275 suggesting that we detected the elementary process of *M. pneumoniae* gliding.
276 The energy conversion efficiencies of stepwise movements are 12%–40%,
277 10%, and 40%–60% for myosin II, cytoplasmic dynein, and kinesin, respectively
278 (26, 45). Previously, we estimated it to be 10%–40% for *M. mobile* gliding (34).
279 These facts suggest that the energy efficiency of stepwise movements of *M.*
280 *pneumoniae* is in a similar range of myosin II and *M. mobile* gliding.
281 **Load-dependent step size.** *M. pneumoniae* cells showed different step
282 sizes depending on the load provided by optical tweezers continuously (Fig. 5I),
283 suggesting that the step size of *M. pneumoniae* is load-dependent. In the
284 infectious process, *M. pneumoniae* cells glide to the deep positions of
285 respiratory systems and experience a large load at these positions (12). The
286 load-dependent stepping behavior would be useful to glide against large loads
287 because a load-independent stepping motor, kinesin, shows frequent back
288 steps under large loads (50, 51). Different step sizes under different loads have
289 also been observed in *M. mobile* gliding (34, 36).
290 **Suggestion for gliding mechanism.** How can we image the gliding
291 mechanism? The GPCA probably plays a critical role in *M. pneumoniae* gliding,
292 because antibodies against the P1 adhesin, a component of GPCA, decreased

293 the gliding speed and ultimately replaced the *M. pneumoniae* cells on the glass
294 surface (40). Recently, the detailed structure of GPCA has been solved (17-20).
295 It is a mushroom structure composed of two P1 adhesins and two P40/P90
296 molecules. The C-terminal regions of the four molecules are bundled and
297 anchored to the cell membrane. P40 and P90 proteins are synthesized as a
298 single protein and processed into two proteins that are not observed in *M.*
299 *genitalium*. Although P1 adhesin is believed to be the receptor for SOs, the
300 binding site exists at the distal end of P40/P90. This complex is thought to
301 undergo conformational changes between open and closed with respect to the
302 binding pockets, which are likely involved in the gliding mechanism (18, 20).
303 The attachment organelle responsible for gliding can be divided into a
304 surface structure including GPCA and an internal rod structure (15, 22, 52-54).
305 Briefly, the force for gliding is likely generated at the bowl because a few
306 proteins essential for gliding and not binding are localized there (55-57). The
307 paired plates and elastic components play a role in force transmission, because
308 the gliding speed decreases severely in a deletion mutant (58). The terminal
309 button likely connects the rod front to the cell membrane, because an end
310 component, the P30 protein, features transmembrane segments (59, 60).
311 Here, we focus on the following observations to construct the working
312 model for the gliding scheme: (1) The force is probably generated around the
313 bowl complex, transmits through the internal structures including paired plates,
314 and reaches GPCAs. (2) Inhibition of cell binding decreases gliding speed. (3)
315 GPCA has open and closed conformations. (4) Gliding can be divided into steps
316 because binding and force are not tightly coupled. (5) The gliding movement

317 can be divided into 14–19 nm steps with a 2.5 pN force.

318 **Gliding scheme to explain stepwise movements.** The model is
319 composed of repeated cycle of four stages (i)–(iv) connected by four steps:
320 “Power stroke,” “Release,” “Displacement,” and “Catch” (Fig. 6). (i) The GPCA
321 in the open state catches an SO on the glass surface. (ii) Contraction of the
322 internal structure pulls the cell body with 2.5 pN and a step size of 14–19 nm.
323 This step is possibly linked to energy from an ATP molecule. (iii) GPCA switches
324 into a closed state by triggering the pulling force transmitted from other working
325 GPCAs, resulting in the release of after-stroke GPCA from the SO. (iv) The
326 released GPCA returns to the open state and displaces another SO in the next
327 position by the extension of the internal structure. (i) The GPCA captures the
328 next SO. The full cycle was then repeated. This scheme explains the
329 relationship between the binding and force of different strains, if we assume that
330 release is enhanced and power stroke and catch are reduced in FH compared
331 with those in M129. The observation that shorter steps occur under load can be
332 explained if we consider that the power stroke is shortened by the load (Fig. 4I).
333 Previously, our group suggested a working model for *M. pneumoniae* gliding,
334 focusing mainly on the information of the internal structure with regard to the
335 attachment organelle (5, 15). The previous model suggested “directed
336 detachment of feet” (GPCA), due to the lack of information about step, force,
337 and foot structure. In this study, we succeeded in adding new information and
338 completing an updated model.

339

340 **Materials and Methods**

341 **Strains and Cultivation.** *M. pneumoniae* M129 (ATCC29342) and FH
342 strains were grown in SP-4 medium at 37°C in tissue culture flasks (TPP
343 Techno Plastic Products AG, Trasadingen, Switzerland), as described
344 previously (11, 61). The FH strain was kindly provided by Tsuyoshi Kenri at the
345 National Institute of Infectious Diseases, Tokyo, Japan.
346 **Optical tweezers system.** An inverted microscope (IX71; Olympus, Tokyo,
347 Japan) was equipped with a Nd:YAG laser (ASF1JE01; Furukawa Electric,
348 Tokyo, Japan) to construct the optical tweezers. The microscope stage was
349 replaced by a piezoelectric stage controlled by a stage controller (MDR14-CA-
350 2.5; SIGMAKOKI, Tokyo, Japan) and a joystick (JS-300; SIGMAKOKI). The
351 irradiated laser beam was concentrated as a finite optical system using a plano-
352 convex lens supported by an optical cage system (SIGMAKOKI). The
353 concentrated laser beam was inserted into the microscope and focused by an
354 objective lens (CFI Apochromat TIRF 100XC Oil; Nikon, Tokyo, Japan). The
355 actual laser power was measured using a power meter (FieldMaxII;
356 COHERENT, Santa Clara, CA) without the objective lens.
357 **Force measurements.** The cell suspension was mixed with 0.5 mM Sulfo-
358 NHS-LC-LC-biotin (Thermo Fisher Scientific, Waltham, MA) as the final
359 concentration and incubated for 15 min at room temperature (RT). The cell
360 suspension was centrifuged at 12,000 × *g* for 10 min, washed with 10 mM
361 HEPES buffer (pH 7.4) containing 150 mM NaCl, centrifuged again, washed
362 with HEPES buffer containing 10% non-heat-inactivated horse serum (Gibco;
363 Thermo Fisher Scientific) and 20 mM glucose, passed through a 0.45-μm pore
364 size filter and incubated for 15 min at RT. The cell suspension was inserted into

365 a tunnel chamber, which was assembled by taping coverslips cleaned with
366 saturated ethanolic KOH and precoated with 100% non-heat-inactivated horse
367 serum for 60 min and 10 mg/ml bovine serum albumin (Sigma-Aldrich, St.
368 Louis, MO) in HEPES buffer for 60 min at RT. The tunnel chamber was washed
369 with HEPES buffer containing 20 mM glucose and incubated at 37°C on optical
370 tweezers equipped with a thermo plate (MATS-OTOR-MV; Tokai Hit, Shizuoka,
371 Japan) and a lens heater (MATS-LH; Tokai Hit). Avidin-conjugated beads in the
372 HEPES buffer containing 20 mM glucose and 0.2–0.3 mM of 3'-*N*-
373 acetylneuraminyllactose (SL) were sonicated and inserted into the tunnel
374 chamber. The avidin-conjugated beads were prepared as previously described
375 (35). The bead movements were recorded using a charge-coupled device
376 (CCD) camera (LRH2500XE-1; DigiMo, Tokyo, Japan) at 30 frames per second
377 and analyzed by displacement of up to 200 nm from the trap center (the linear
378 range of the laser trap) using ImageJ 1.43u (http://rsb.info.nih.gov/ij/) and IGOR
379 Pro 6.33 J and 8.02 J (WaveMetrics, Portland, OR) (34, 35, 62).
380 **Binding and gliding analyses.** Cultured cells were washed with buffer in a
381 culture flask, and then washed with HEPES buffer containing 10% non-heat-
382 inactivated horse serum (Gibco; Thermo Fisher Scientific) and 20 mM glucose.
383 Cultured cells were scraped off the culture flask, passed through a 0.45-μm
384 pore size filter, and incubated for 15 min at RT. The cell suspension was then
385 inserted into the tunnel chamber. The tunnel chamber was washed with HEPES
386 buffer containing 20 mM glucose, incubated at 37°C on an inverted microscope
387 (IX83; Olympus) equipped with a thermo plate and lens heater, observed by
388 phase-contrast microscopy at 37°C, and recorded with a CCD camera (DMK

389 33UX174; The Imaging Source Asia Co. Ltd., Taiepi City, Taiwan). Then, the
390 tunnel chamber was washed with HEPES buffer containing 20 mM glucose and
391 various concentrations of SL. Video data were analyzed using ImageJ 1.43u
392 and IGOR Pro 6.33 J.

393 **Genome sequencing and variant analyses.** Frozen stocks of cells were
394 plated on Aluotto medium and isolated as previously described (63). Genomic
395 DNA was isolated and sequenced using MiSeq (Illumina, San Diego, CA), as
396 previously described (34). Sequence read mapping and variant detection were
397 performed using the CLC Genomics Workbench (QIAGEN, Hilden, Germany).
398

399 Acknowledgments

400 We thank Dr. Tsuyoshi Kenri at the National Institute of Infectious Diseases and
401 Dr. Ikuko Fujiwara at Osaka City University for helpful discussions, and Dr.
402 Shigeyuki Kakizawa at the National Institute of Advanced Industrial Science and
403 Technology (AIST) for supporting the genome sequence analyses. This work
404 was supported by Grants-in-Aid for Scientific Research: (A) (MEXT KAKENHI
405 Grant Numbers JP24390107, JP17H01544) and by JST CREST (Grant Number
406 JPMJCR19S5, Japan). M. Mizutani is the recipient of a Research Fellowship of
407 the Japan Society for the Promotion of Science (18J15362).
408

409 References

410 1. Razin S, Yogev D, Naot Y. 1998. Molecular biology and pathogenicity of
411 mycoplasmas. Microbiol Mol Biol Rev 62:1094-156.
412 2. Razin S, Hayflick L. 2010. Highlights of mycoplasma research--an historical

413 perspective. Biologicals 38:183-90.
414 3. Miyata M, Robinson RC, Uyeda TQP, Fukumori Y, Fukushima SI, Haruta S,
415 Homma M, Inaba K, Ito M, Kaito C, Kato K, Kenri T, Kinosita Y, Kojima S,
416 Minamino T, Mori H, Nakamura S, Nakane D, Nakayama K, Nishiyama M,
417 Shibata S, Shimabukuro K, Tamakoshi M, Taoka A, Tashiro Y, Tulum I,
418 Wada H, Wakabayashi KI. 2020. Tree of motility - A proposed history of
419 motility systems in the tree of life. Genes Cells 25:6-21.
420 4. Miyata M, Hamaguchi T. 2016. Prospects for the gliding mechanism of
421 *Mycoplasma mobile*. Curr Opin Microbiol 29:15-21.
422 5. Miyata M, Hamaguchi T. 2016. Integrated information and prospects for
423 gliding mechanism of the pathogenic bacterium *Mycoplasma pneumoniae*.
424 Front Microbiol 7:960.
425 6. Saraya T. 2017. *Mycoplasma pneumoniae* infection: Basics. J Gen Fam
426 Med 18:118-125.
427 7. Nagai R, Miyata M. 2006. Gliding motility of *Mycoplasma mobile* can occur
428 by repeated binding to *N*-acetylneuraminyllactose (sialyllactose) fixed on
429 solid surfaces. J Bacteriol 188:6469-75.
430 8. Varki A. 2008. Sialic acids in human health and disease. Trends Mol Med
431 14:351-60.
432 9. Kasai T, Nakane D, Ishida H, Ando H, Kiso M, Miyata M. 2013. Role of
433 binding in *Mycoplasma mobile* and *Mycoplasma pneumoniae* gliding
434 analyzed through inhibition by synthesized sialylated compounds. J
435 Bacteriol 195:429-35.
436 10. Williams CR, Chen L, Driver AD, Arnold EA, Sheppard ES, Locklin J,
437 Krause DC. 2018. Sialylated receptor setting influences *Mycoplasma*
438 *pneumoniae* attachment and gliding motility. Mol Microbiol 109:735-744.
439 11. Nakane D, Miyata M. 2009. Cytoskeletal asymmetrical dumbbell structure of
440 a gliding mycoplasma, *Mycoplasma gallisepticum*, revealed by negative-
441 staining electron microscopy. J Bacteriol 191:3256-64.
442 12. Prince OA, Krunkosky TM, Krause DC. 2014. In vitro spatial and temporal
443 analysis of *Mycoplasma pneumoniae* colonization of human airway
444 epithelium. Infect Immun 82:579-86.
445 13. Seto S, Layh-Schmitt G, Kenri T, Miyata M. 2001. Visualization of the
446 attachment organelle and cytadherence proteins of *Mycoplasma*
447 *pneumoniae* by immunofluorescence microscopy. J Bacteriol 183:1621-30.
448 14. Nakane D, Kenri T, Matsuo L, Miyata M. 2015. Systematic structural

449 analyses of attachment organelle in *Mycoplasma pneumoniae*. PLoS
450 Pathog 11:e1005299.
451 15. Kawamoto A, Matsuo L, Kato T, Yamamoto H, Namba K, Miyata M. 2016.
452 Periodicity in attachment organelle revealed by electron cryotomography
453 suggests conformational changes in gliding mechanism of *Mycoplasma*
454 *pneumoniae*. MBio 7:e00243-16.
455 16. Nakane D, Adan-Kubo J, Kenri T, Miyata M. 2011. Isolation and
456 characterization of P1 adhesin, a leg protein of the gliding bacterium
457 *Mycoplasma pneumoniae*. J Bacteriol 193:715-22.
458 17. Aparicio D, Torres-Puig S, Ratera M, Querol E, Pinol J, Pich OQ, Fita I.
459 2018. *Mycoplasma genitalium* adhesin P110 binds sialic-acid human
460 receptors. Nat Commun 9:4471.
461 18. Aparicio D, Scheffer MP, Marcos-Silva M, Vizarraga D, Sprankel L, Ratera
462 M, Weber MS, Seybert A, Torres-Puig S, Gonzalez-Gonzalez L, Reitz J,
463 Querol E, Pinol J, Pich OQ, Fita I, Frangakis AS. 2020. Structure and
464 mechanism of the Nap adhesion complex from the human pathogen
465 *Mycoplasma genitalium*. Nat Commun 11:2877.
466 19. Vizarraga D, Kawamoto A, Matsumoto U, Illanes R, Perez-Luque R, Martin
467 J, Mazzolini R, Bierge P, Pich OQ, Espasa M, Sanfeliu I, Esperalba J,
468 Fernandez-Huerta M, Scheffer MP, Pinyol J, Frangakis AS, Lluch-Senar M,
469 Mori S, Shibayama K, Kenri T, Kato T, Namba K, Fita I, Miyata M, Aparicio
470 D. 2020. Immunodominant proteins P1 and P40/P90 from human pathogen
471 *Mycoplasma pneumoniae*. Nat Commun 11:5188.
472 20. Vizarraga D, Torres-Puig S, Aparicio D, Pich OQ. 2021. The sialoglycan
473 binding adhesins of *Mycoplasma genitalium* and *Mycoplasma pneumoniae*.
474 Trends Microbiol 29:477-481.
475 21. Miyata M. 2008. Centipede and inchworm models to explain *Mycoplasma*
476 gliding. Trends Microbiol 16:6-12.
477 22. Seybert A, Gonzalez-Gonzalez L, Scheffer MP, Lluch-Senar M, Mariscal
478 AM, Querol E, Matthaeus F, Pinol J, Frangakis AS. 2018. Cryo-electron
479 tomography analyses of terminal organelle mutants suggest the motility
480 mechanism of *Mycoplasma genitalium*. Mol Microbiol 108:319-329.
481 23. Mizutani M, Miyata M. 2019. Behaviors and energy source of *Mycoplasma*
482 *gallisepticum* gliding. J Bacteriol 201:e00397-19.
483 24. Schnitzer MJ, Block SM. 1997. Kinesin hydrolyses one ATP per 8-nm step.
484 Nature 388:386-90.

485 25. Tanaka H, Homma K, Iwane AH, Katayama E, Ikebe R, Saito J, Yanagida T,
486 Ikebe M. 2002. The motor domain determines the large step of myosin-V.
487 Nature 415:192-5.
488 26. Mallik R, Carter BC, Lex SA, King SJ, Gross SP. 2004. Cytoplasmic dynein
489 functions as a gear in response to load. Nature 427:649-52.
490 27. Sowa Y, Rowe AD, Leake MC, Yakushi T, Homma M, Ishijima A, Berry RM.
491 2005. Direct observation of steps in rotation of the bacterial flagellar motor.
492 Nature 437:916-9.
493 28. Veigel C, Coluccio LM, Jontes JD, Sparrow JC, Milligan RA, Molloy JE.
494 1999. The motor protein myosin-I produces its working stroke in two steps.
495 Nature 398:530-3.
496 29. Kojima H, Muto E, Higuchi H, Yanagida T. 1997. Mechanics of single kinesin
497 molecules measured by optical trapping nanometry. Biophys J 73:2012-22.
498 30. Merz AJ, So M, Sheetz MP. 2000. Pilus retraction powers bacterial twitching
499 motility. Nature 407:98-102.
500 31. Takagi Y, Homsher EE, Goldman YE, Shuman H. 2006. Force generation in
501 single conventional actomyosin complexes under high dynamic load.
502 Biophys J 90:1295-307.
503 32. Gennerich A, Carter AP, Reck-Peterson SL, Vale RD. 2007. Force-induced
504 bidirectional stepping of cytoplasmic dynein. Cell 131:952-65.
505 33. Miyata M, Ryu WS, Berg HC. 2002. Force and velocity of *Mycoplasma*
506 *mobile* gliding. J Bacteriol 184:1827-31.
507 34. Mizutani M, Tulum I, Kinosita Y, Nishizaka T, Miyata M. 2018. Detailed
508 analyses of stall force generation in *Mycoplasma mobile* gliding. Biophys J
509 114:1411-9.
510 35. Mizutani M, Miyata M. 2017. Force measurement on *Mycoplasma mobile*
511 gliding using optical tweezers. Bio Protoc 7:e2127.
512 36. Kinosita Y, Nakane D, Sugawa M, Masaike T, Mizutani K, Miyata M,
513 Nishizaka T. 2014. Unitary step of gliding machinery in *Mycoplasma mobile*.
514 Proc Natl Acad Sci USA 111:8601-6.
515 37. Pelicic V. 2008. Type IV pili: *e pluribus unum*? Mol Microbiol 68:827-37.
516 38. Clausen M, Jakovljevic V, Sogaard-Andersen L, Maier B. 2009. High-force
517 generation is a conserved property of type IV pilus systems. J Bacteriol
518 191:4633-8.
519 39. Hatchel JM, Balish MF. 2008. Attachment organelle ultrastructure correlates
520 with phylogeny, not gliding motility properties, in *Mycoplasma pneumoniae*

521 relatives. Microbiology 154:286-95.
522 40. Seto S, Kenri T, Tomiyama T, Miyata M. 2005. Involvement of P1 adhesin in
523 gliding motility of *Mycoplasma pneumoniae* as revealed by the inhibitory
524 effects of antibody under optimized gliding conditions. J Bacteriol 187:1875-
525 7.
526 41. Rosengarten R, Fischer M, Kirchhoff H, Kerlen G, Seack KH. 1988.
527 Transport of erythrocytes by gliding cells of *Mycoplasma mobile* 163K.
528 Current Microbiology 16:253-7.
529 42. Uenoyama A, Kusumoto A, Miyata M. 2004. Identification of a 349-
530 kilodalton protein (Gli349) responsible for cytadherence and glass binding
531 during gliding of *Mycoplasma mobile*. J Bacteriol 186:1537-45.
532 43. Uenoyama A, Seto S, Nakane D, Miyata M. 2009. Regions on Gli349 and
533 Gli521 protein molecules directly involved in movements of *Mycoplasma*
534 *mobile* gliding machinery, suggested by use of inhibitory antibodies and
535 mutants. J Bacteriol 191:1982-5.
536 44. Nishikawa MS, Nakane D, Toyonaga T, Kawamoto A, Kato T, Namba K,
537 Miyata M. 2019. *Mycoplasma mobile* gliding based on structure, ATPase
538 activity, and sialic acid binding of machinery. MBio 10:e02846-19.
539 45. Bustamante C, Chemla YR, Forde NR, Izhaky D. 2004. Mechanical
540 processes in biochemistry. Annu Rev Biochem 73:705-48.
541 46. Fujita K, Iwaki M, Iwane AH, Marcucci L, Yanagida T. 2012. Switching of
542 myosin-V motion between the lever-arm swing and brownian search-and-
543 catch. Nat Commun 3:956.
544 47. Park PJ, Lee KJ. 2013. A modified active Brownian dynamics model using
545 asymmetric energy conversion and its application to the molecular motor
546 system. J Biol Phys 39:439-52.
547 48. Nakamura S, Kami-ike N, Yokota JP, Minamino T, Namba K. 2010.
548 Evidence for symmetry in the elementary process of bidirectional torque
549 generation by the bacterial flagellar motor. Proc Natl Acad Sci U S A
550 107:17616-20.
551 49. Yasuda R, Noji H, Kinosita K, Jr., Yoshida M. 1998. F_1-ATPase is a highly
552 efficient molecular motor that rotates with discrete 120 degree steps. Cell
553 93:1117-24.
554 50. Carter NJ, Cross RA. 2006. Kinesin's moonwalk. Curr Opin Cell Biol 18:61-
555 7.
556 51. Toleikis A, Carter NJ, Cross RA. 2020. Backstepping mechanism of kinesin-

1. Biophys J 119:1984-1994.
52. Henderson GP, Jensen GJ. 2006. Three-dimensional structure of *Mycoplasma pneumoniae*'s attachment organelle and a model for its role in gliding motility. Mol Microbiol 60:376-85.
53. Seybert A, Herrmann R, Frangakis AS. 2006. Structural analysis of *Mycoplasma pneumoniae* by cryo-electron tomography. J Struct Biol 156:342-54.
54. Krause DC, Chen S, Shi J, Jensen AJ, Sheppard ES, Jensen GJ. 2018. Electron cryotomography of *Mycoplasma pneumoniae* mutants correlates terminal organelle architectural features and function. Mol Microbiol 108:306-318.
55. Hasselbring BM, Jordan JL, Krause DC. 2005. Mutant analysis reveals a specific requirement for protein P30 in *Mycoplasma pneumoniae* gliding motility. J Bacteriol 187:6281-9.
56. Jordan JL, Chang HY, Balish MF, Holt LS, Bose SR, Hasselbring BM, Waldo RH, 3rd, Krunkosky TM, Krause DC. 2007. Protein P200 is dispensable for *Mycoplasma pneumoniae* hemadsorption but not gliding motility or colonization of differentiated bronchial epithelium. Infect Immun 75:518-22.
57. Kawakita Y, Kinoshita M, Furukawa Y, Tulum I, Tahara YO, Katayama E, Namba K, Miyata M. 2016. Structural study of MPN387, an essential protein for gliding motility of a human-pathogenic bacterium, *Mycoplasma pneumoniae*. J Bacteriol 198:2352-9.
58. Garcia-Morales L, Gonzalez-Gonzalez L, Querol E, Pinol J. 2016. A minimized motile machinery for *Mycoplasma genitalium*. Mol Microbiol 100:125-38.
59. Chang HY, Jordan JL, Krause DC. 2011. Domain analysis of protein P30 in *Mycoplasma pneumoniae* cytadherence and gliding motility. J Bacteriol 193:1726-33.
60. Relich RF, Balish MF. 2011. Insights into the function of *Mycoplasma pneumoniae* protein P30 from orthologous gene replacement. Microbiology (Reading) 157:2862-2870.
61. Tully JG. 1983. New laboratory techniques for isolation of *Mycoplasma pneumoniae*. Yale J Biol Med 56:511-5.
62. Tanaka A, Nakane D, Mizutani M, Nishizaka T, Miyata M. 2016. Directed binding of gliding bacterium, *Mycoplasma mobile*, shown by detachment force and bond lifetime. MBio 7:e00455-16.

63. Tulum I, Yabe M, Uenoyama A, Miyata M. 2014. Localization of P42 and F_1-ATPase alpha-subunit homolog of the gliding machinery in *Mycoplasma mobile* revealed by newly developed gene manipulation and fluorescent protein tagging. J Bacteriol 196:1815-24.

599 # Figures

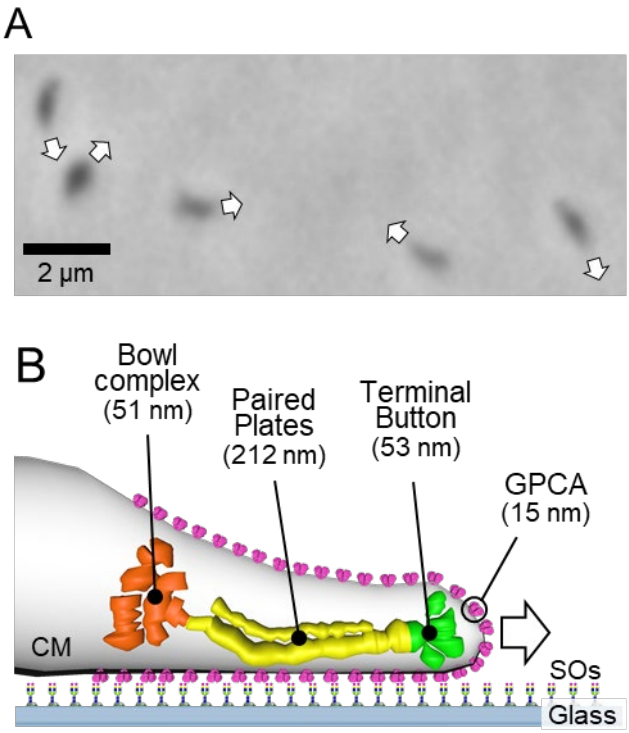

600

601

602 **FIG 1. Gliding motility of *Mycoplasma pneumoniae*.** (A) Phase-contrast
603 micrograph of *M. pneumoniae* cells. The gliding directions of cells are indicated
604 by white arrows. (B) Illustration of gliding machinery. The gliding machinery is
605 composed of the bowl complex, paired plates, terminal button, and GPCA. The
606 lengths along the cell axis are summarized from previous studies (14, 19).
607 GPCA, working as a leg, is anchored to the cell membrane (CM) and catches
608 sialylated oligosaccharides (SOs) fixed on solid surfaces.

609

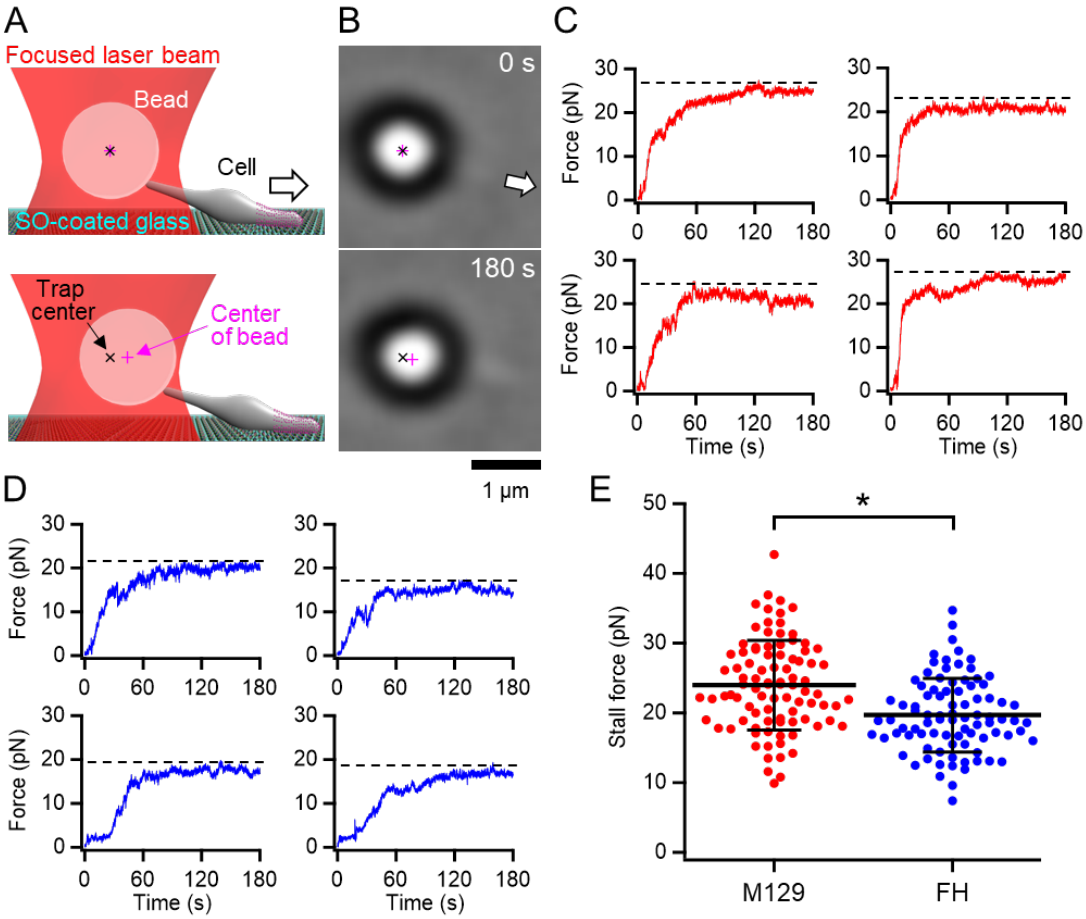

610

611

612 **FIG 2. Stall force measurements.** (A) Illustrations of experimental design for

613 force measurements. The white arrow indicates the gliding direction. (B) Optical

614 micrographs of a trapped cell. The cell attached with a bead (large black ring

615 with white center) glided in the direction of the white arrow from 0 and stalled in

616 180 s. The cell image can be observed near the base of the arrow. (C) Four

617 representative time courses of force increments for M129 strain. The broken

618 lines indicate the values of stall force. (D) Four representative time courses of

619 force increments for FH strain. The broken lines indicate the values of stall

620 force. (E) Scatter dot plot of stall force (*n* = 92 and 88 in M129 and FH,

621 respectively) shown with averages (thick lines) and standard deviations (thin

622 lines). *$p = 2.4\times10^{-6}$ by Student's *t*-test.

623

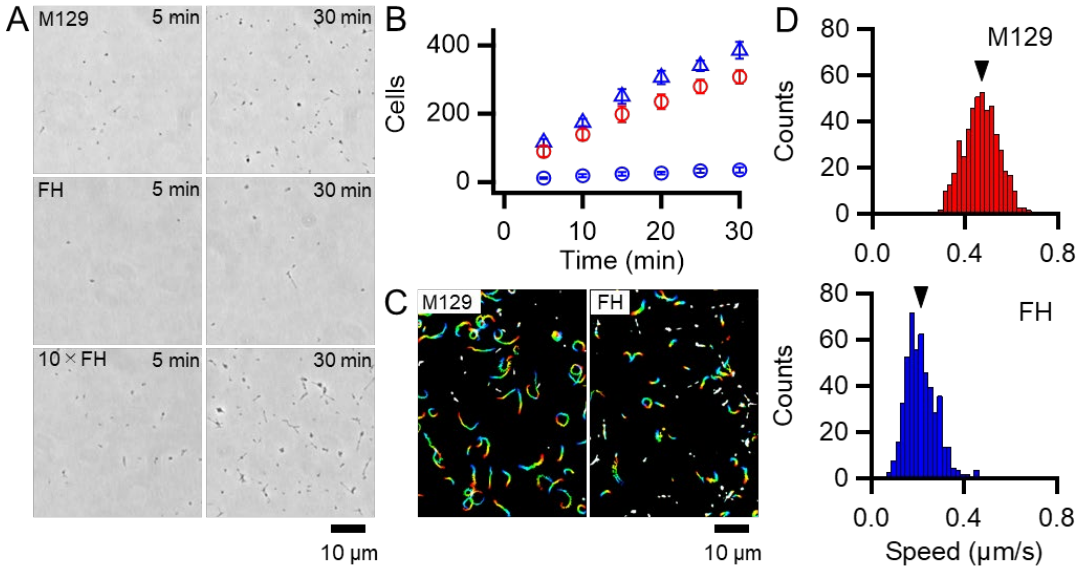

FIG 3. Binding activity and gliding motility. (A) Phase-contrast micrographs of cells on SO-coated glass surfaces. M129, FH, and 10× concentrated FH are shown after 5 and 30 min of incubation. (B) Averaged bound cell numbers in 100×100 μm^2 plotted with standard deviations (n = 10 in each). M129 (red open circle), FH (blue open circle), and 10× concentrated FH (blue open triangle) are presented. (C) Cell trajectories for 20 s, changing color with time from red to blue. (D) Distributions of gliding speeds averaged for 20 s at 1-s intervals (n = 500 in each). Mean values are marked by black triangles.

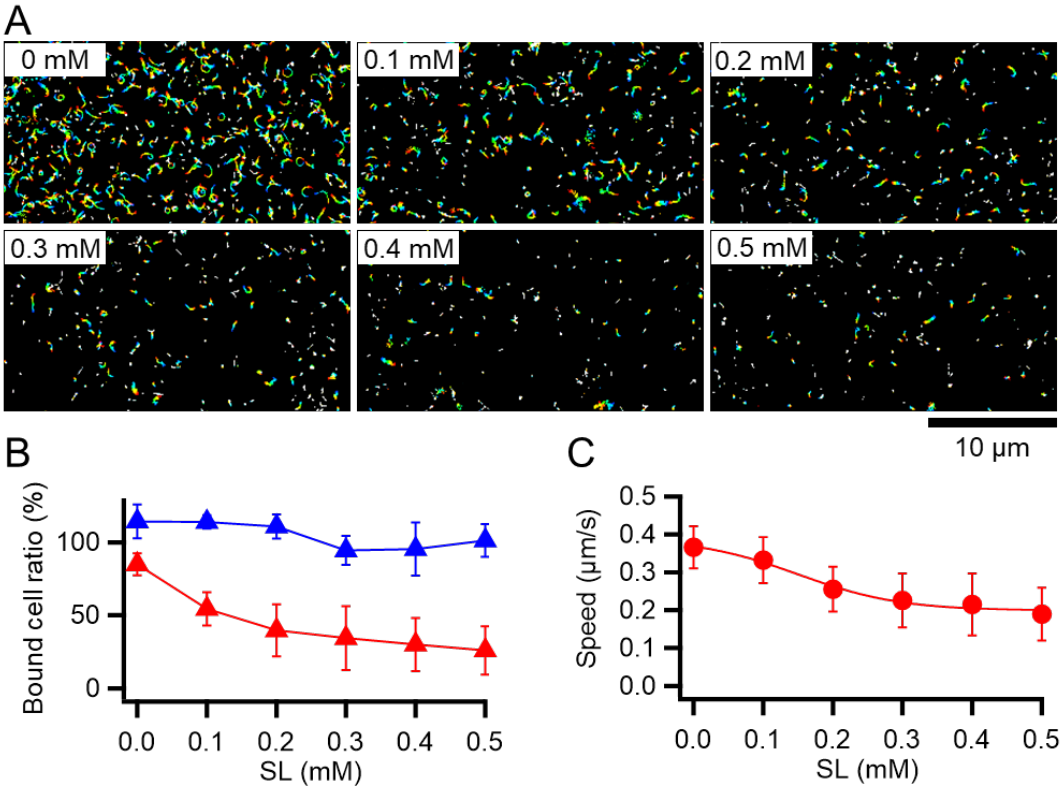

FIG 4. Effects of SL on binding and gliding. (A) Gliding cells were treated with free SL. The cell trajectories after SL treatment are presented as a stack for 20 s, changing color from red to blue. SL concentrations are shown at the left upper corner of each panel. (B) Number of cells bound to the glass at 5 min after treatment are plotted relative to the initial cell number. The averages for gliding (red triangles) and non-gliding (blue triangles) cells are shown with the standard deviations (n = 10, 10, 10, 10, 9, and 10 for 0, 0.1, 0.2, 0.3, 0.4, and 0.5 mM, respectively). (C) Averaged gliding speeds under various SL concentrations are plotted with the standard deviations and fitted by a sigmoidal curve (n = 50, 50, 50, 50, 56, and 56 for 0, 0.1, 0.2, 0.3, 0.4, and 0.5 mM, respectively).

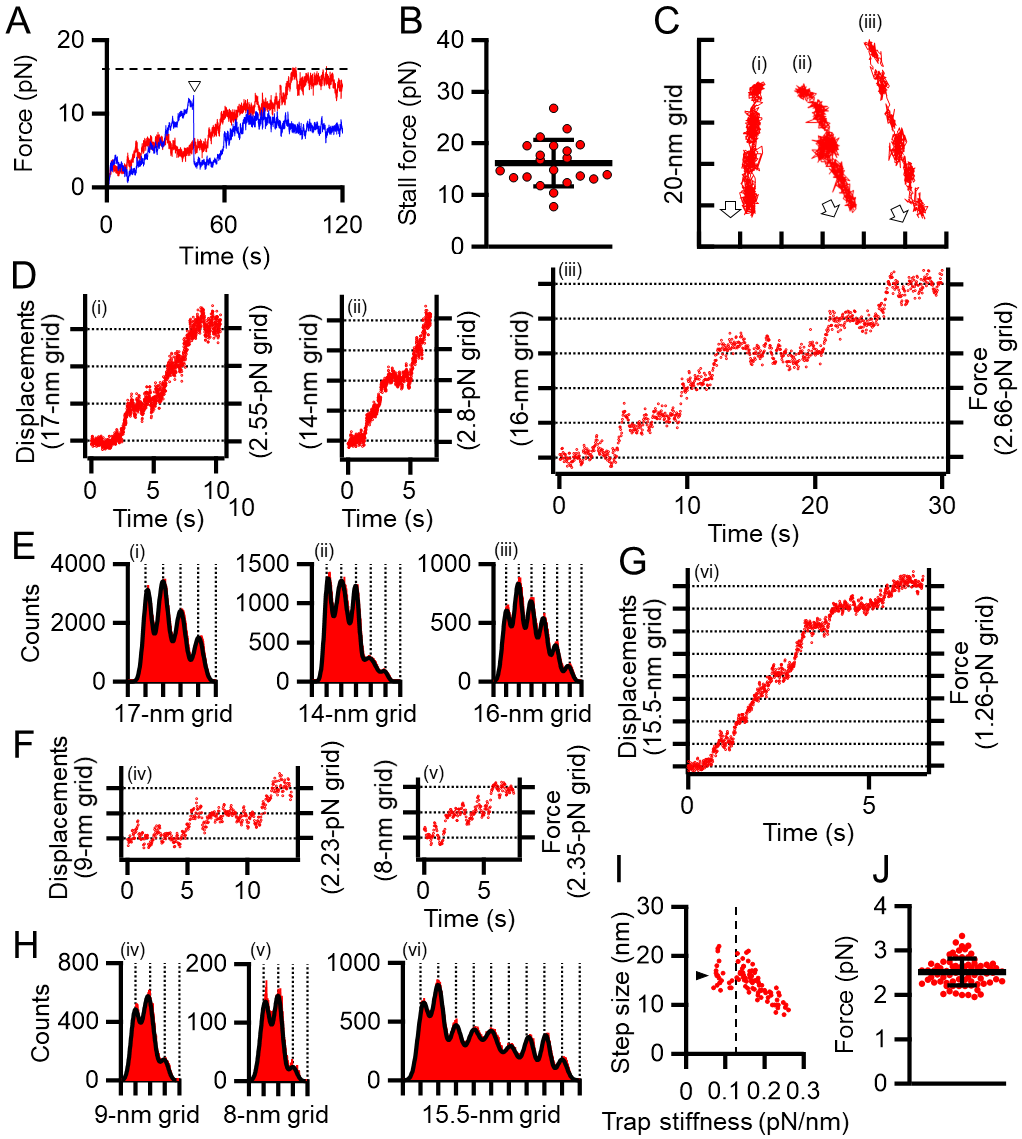

FIG 5. Stepwise movements under SL. (A) Representative force traces with time under 0.2–0.3 mM SL are shown for stalled (red) and detached (blue) cells. The broken line indicates the stall force. The time point of detachment is marked by a triangle. (B) Scatter dot plot of stall force shown with averages (thick line) and standard deviations (thin lines) (n = 21). (C) Three cell trajectories with stepwise movements are shown in a field. Open arrows indicate the gliding direction. (D) Displacement and force of cells whose

trajectories are shown in panel (C). (E) Histograms of pairwise distance function (PDF) analysis of panel (D) were fitted by the sum of Gaussian curves. (F) Displacement and force under high trap stiffness. (G) Displacement and force under low trap stiffness. (H) Histograms of PDF analysis of panel (F) and (G). (I) Distribution of step size under various trap stiffnesses. Step sizes were plotted as a function of trap stiffness (n = 97). The position at 0.12 pN/nm of trap stiffness was marked by a dotted line. The average of step size under 0.07–0.12 pN/nm of trap stiffness was marked by a triangle. (J) Scatter dot plot of force increments under 0.13–0.26 pN/nm of trap stiffness shown with averages (thick line) and standard deviations (thin lines) (n = 76).

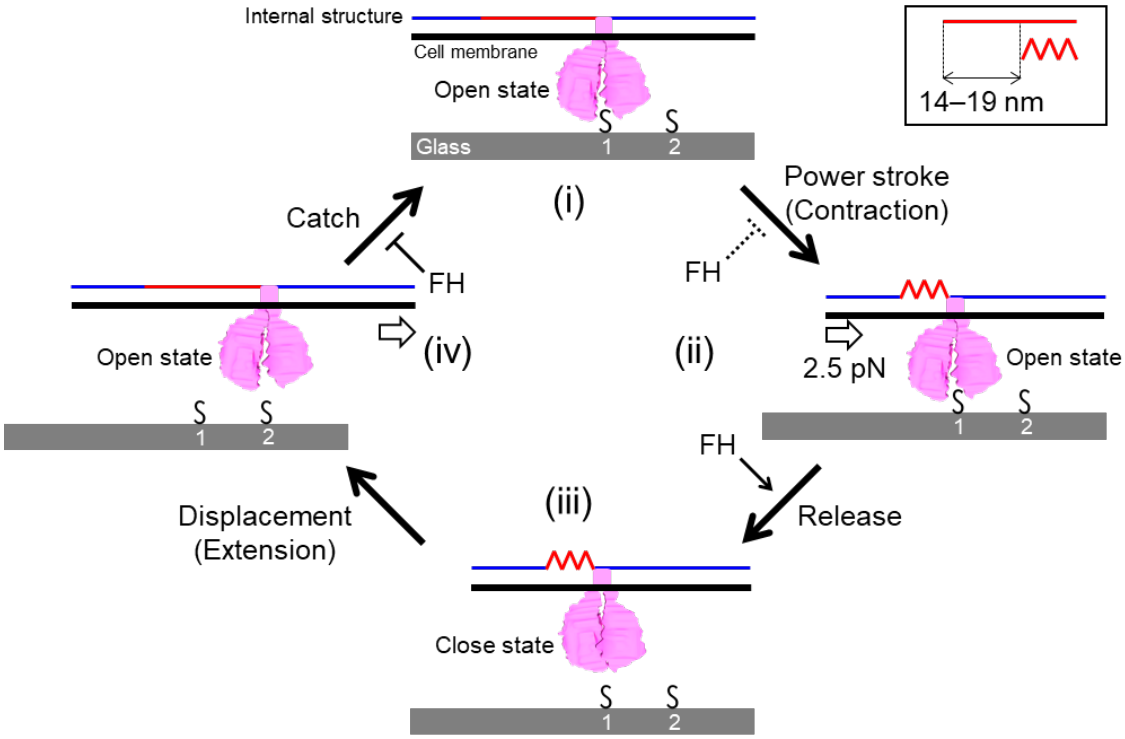

FIG 6. Schematic illustration of leg behaviors in stepwise movements. Internal structure, represented by blue and red lines, is responsible for force transmission. It repeats contraction and extension cooperatively with the surface structures. Conformational change of internal structure and step size are shown in the right-upper box. GPCA is presented in pink. Sialylated oligosaccharides are shown by “S.” Force exerted in a step is shown by an arrow in panel (ii). Displacement of the cell body forward is shown by an arrow in panel (iv). The gliding occurs through stages i to iv. See text for details.